


## Structure and glide of Lomer and Lomer-Cottrell dislocations: Atomistic simulations for model concentrated alloy solid solutions

Anas Abu-Odeh <sup>1,2</sup>, Tarun Allaparti <sup>1</sup> and Mark Asta <sup>1,2,\*</sup>

<sup>1</sup>*Department of Materials Science and Engineering, University of California, Berkeley, California 94720, USA*

<sup>2</sup>*Materials Sciences Division, Lawrence Berkeley National Laboratory, Berkeley, California 94720, USA*

 (Received 5 July 2022; revised 5 October 2022; accepted 17 October 2022; published 31 October 2022)

Lomer (L) and Lomer-Cottrell (LC) dislocations have long been considered to be central to work hardening in face-centered cubic (FCC) metals and alloys. These dislocations act as barriers of motion for other dislocations, and can serve as sites for twin nucleation. Recent focus on multicomponent concentrated FCC solid solution alloys has resulted in many reported observations of LC dislocations. While these and L dislocations are expected to have a role in the mechanical behavior of these alloys, little is understood about how variations in composition and associated fault energies change the response of these dislocations under stress. We present atomistic simulations of L and LC dislocations in a model Cu-Ni system and find that changes in composition and applied stress conditions result in a wide variety of responses, including changes in core configuration and (100) glide. The results are compared to and extend previous literature related to the nature of L/LC core structures and how they vary with respect to intrinsic materials properties and stress states. This study also provides insights into mechanisms such as twin nucleation that could have important implications for work hardening in FCC solid-solution alloys.

DOI: [10.1103/PhysRevMaterials.6.103603](https://doi.org/10.1103/PhysRevMaterials.6.103603)

### I. INTRODUCTION

Understanding the stability of Lomer (L) and Lomer-Cottrell (LC) dislocations is crucial for insight into a variety of deformation and microstructural behaviors in face-centered cubic (FCC) metals and alloys. L and LC dislocations have historically been proposed as major contributors to work hardening in these systems [1–3], which is a property that has been shown to depend on stress orientation in single crystal tensile tests [4,5]. Recent transmission electron microscope (TEM) observations of deformed FCC high-entropy alloys have reported the presence of LC dislocations [6–10], suggesting that these dislocations may play a role in the properties of these alloys. LC dislocations have also been considered as possible twin nucleation sites [11–13], which can increase ductility and strength (e.g., through a dynamic Hall-Petch effect). Additionally, glide of L dislocations in the (100) plane could aid in deformation at higher temperatures through direct motion of L dislocations [14] or through L dislocations acting as kink pairs for a screw dislocation dissociated on a compact plane migrating in a (100) plane [15]. A reaction involving a L dislocation has previously been used to explain the motion of a low-angle  $\langle 110 \rangle$  tilt boundary in FCC aluminum [16]. The results summarized here are representative of previous literature that clearly demonstrate the important role of L and LC dislocations in the deformation behavior and microstructures of FCC metals and alloys.

Lomer and Lomer-Cottrell dislocations are formed by the reaction of a  $60^\circ$  mixed dislocation with a Burgers vector of

$\frac{a}{2}[\bar{1}10]$  on the (111) plane with another  $60^\circ$  mixed dislocation with a Burgers vector of  $\frac{a}{2}[101]$  on the  $(\bar{1}\bar{1}1)$  plane [Fig. 1(a)], where  $a$  is the FCC lattice constant [17]. The L dislocation is formed through the reaction of the  $60^\circ$  mixed dislocations at the intersection of the (111) and  $(\bar{1}\bar{1}1)$  planes to form a dislocation with a  $\frac{a}{2}[011]$  Burgers vector and line direction along  $[0\bar{1}1]$  [Fig. 1(b)]:

$$\frac{a}{2}[\bar{1}10] + \frac{a}{2}[101] \rightarrow \frac{a}{2}[011]. \quad (1)$$

The (100) glide plane of the L product dislocation is not a closed-packed plane, and will thus have a higher barrier for glide than dislocations gliding on the  $\{111\}$  planes. The L dislocation thus acts as an obstacle for subsequent dislocations gliding on the intersecting (111) and  $(\bar{1}\bar{1}1)$  planes.

In the FCC crystal structure, the  $60^\circ$  mixed dislocations will dissociate into two Shockley partial dislocations bounding a stacking fault [Fig. 1(c)] through the following reactions:

$$\frac{a}{2}[\bar{1}10] \rightarrow \frac{a}{6}[\bar{1}2\bar{1}] + \frac{a}{6}[\bar{2}11], \quad (2)$$

$$\frac{a}{2}[101] \rightarrow \frac{a}{6}[1\bar{1}2] + \frac{a}{6}[211]. \quad (3)$$

An alternative reaction to Eq. (1), with the same net Burgers vector, can be written as

$$\begin{aligned} & \frac{a}{6}[\bar{1}2\bar{1}] + \frac{a}{6}[1\bar{1}2] + \frac{a}{6}[\bar{2}11] + \frac{a}{6}[211] \\ & \rightarrow \frac{a}{6}[011] + \frac{a}{6}[\bar{2}11] + \frac{a}{6}[211]. \end{aligned} \quad (4)$$

\*mdasta@berkeley.edu

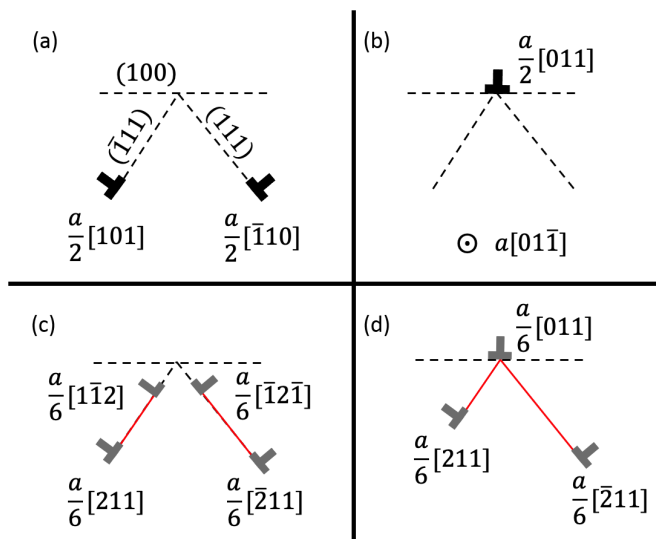


FIG. 1. (a) Two perfect 60° mixed dislocations lying on intersecting {111} planes. (b) A Lomer dislocation on a (100) plane. (c) Two dissociated 60° mixed dislocations lying on intersecting {111} planes. (d) A Lomer-Cottrell dislocation. Black symbols represent perfect dislocations, grey symbols represent partial dislocations, and red lines represent intrinsic stacking faults. The circled dot in (b) represents the direction out of the page.

The product configuration of Eq. (4) is the LC dislocation [Fig. 1(d)] with the reactants being partial dislocations from the two 60° mixed dislocations. The leading partial dislocations of the two 60° mixed dislocations form a sessile stair-rod partial dislocation with a Burgers vector of  $\frac{a}{6}[011]$ . This dislocation is connected to the other two partial dislocations through stacking faults on the intersecting closed-packed planes. The LC configuration is conventionally considered to be a stronger barrier than the compact L dislocation against subsequent dislocation motion due to the sessile nature of the stair-rod partial dislocation.

While dislocations tend to be dissociated in FCC crystal structures, the LC dislocation is not guaranteed to form from two dissociated 60° mixed dislocations. It is possible to form the L dislocation instead. Predicting the product configuration from linear elasticity theory is difficult without the knowledge of dislocation core energies [18,19]. Alternatively, the core configuration can be directly modeled through atomistic simulations.

Previous linear elasticity-based analyses on these dislocations, while lacking consideration of the dislocation core, have resulted in useful insights. Linear elasticity theory, with either anisotropic [20] or isotropic [21] elastic constants, has been used to predict an asymmetrical dissociation of LC dislocations across the closed-packed planes, a conclusion that was later verified with atomistic simulations [19]. Stroh [22] has proposed that under an applied stress it may be possible for a LC dislocation to have its partial dislocations recombine into a L dislocation to glide in a (100) plane or that it may decompose into the reactant dislocations from which it was formed. An anisotropic linear elasticity-based dislocation dynamics model of a LC junction in FCC metals and its response to stress through an unzipping mechanism [23], which causes the

L/LC configuration to decompose into its parent dislocations, was able to replicate many of the details of a quasicontinuum method that treated atoms near the junction with an interatomic potential [24]. This led the authors of the former study to conclude that knowledge of elastic interactions and stacking fault energy is all that is needed to determine the junction structure. Challenges are associated with extending such analyses, as described above. Specifically, it is difficult to predict if the L or LC configuration is lower in energy without knowledge of core energies [18,19], contrary to suggestions of previous authors [23]. The importance of the core structure is also emphasized by Stroh [22] in the context of possible transformations of a LC dislocation. Further understanding of L and LC dislocations, and by extension their role in the mechanical properties of FCC metals and alloys, thus requires an accurate description of the dislocation core structure.

Specifically, it is important to understand how a variation in composition affects the resistance of a L or LC dislocation against glide, which gives a measure of their capacity to harden the material by blocking the glide of other dislocations. Further, it is important to understand how composition affects the different possible core transformations, such as the nucleation of a nanotwin, that can occur. These core transformations can result in further hardening of the material, especially if they produce faults that intersect glide planes. In addition, understanding the stress orientation dependence of glide resistance and core transformations may reveal insights into the orientation dependence of work hardening in FCC alloys. While the previously mentioned unzipping mechanism has been studied as a stress-induced response of these dislocations [23,24], additional responses are expected to occur. Evidence for this is present in the form of TEM studies of glide dislocations on (100) planes in high- [25] and low- [26] stacking fault energy FCC alloys. In the latter case, a constriction of a LC dislocation to a L dislocation is expected to occur to facilitate glide. The competition between these (and potentially other) responses is likely due to a combination of pinning, line tension, stress field, and core structure effects.

Motivated by these questions, we undertake in this paper the modeling of L and LC dislocations through atomistic simulations using elastic- and lattice-Green's-function flexible boundary conditions in a Cu-Ni average-atom system described by an embedded-atom method (EAM) potential [27,28]. The equilibrium structure of these dislocations are surveyed under different compositions, shear stress orientations, and magnitudes to probe their resistance to glide and different possible core transformations. We find that depending on the shear stress orientation, the relative resistance against glide on a (100) plane is not solely due to the relative value of the unstable stacking-fault energy on that plane. Additionally, core transformations involving faults can occur for materials with both low (Cu-rich compositions) and high (Ni-rich compositions) fault energies, depending on the orientation and magnitude of the stress field. The paper presented here thus represents a systematic study of L and LC dislocations as a function of composition and stress orientation that extends previous atomistic and continuum studies of this topic.

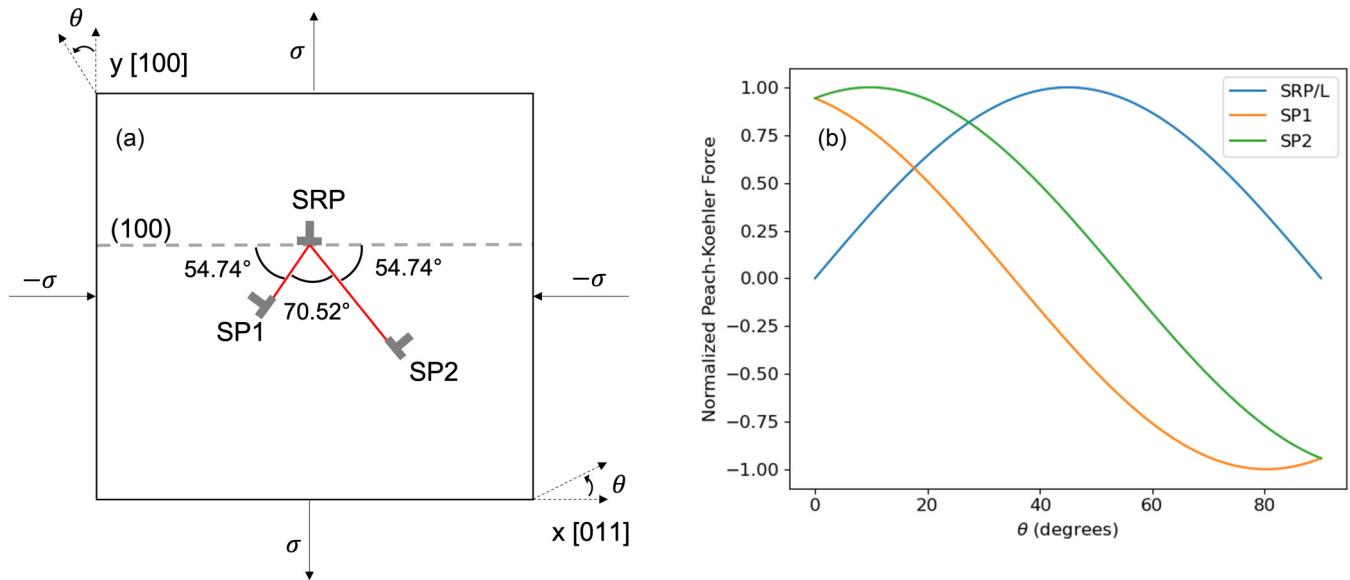


FIG. 2. (a) Schematic of a LC configuration under pure shear. Partial dislocations are represented by grey half crosses and intrinsic stacking faults are represented by red lines. The directions are given in the crystal basis. (b) Normalized Peach-Koehler (P-K) forces for partial dislocations in (a) as a function of  $\theta$ . The meaning of the sign of the P-K forces is given in the text.

## II. MODEL AND METHODS

### A. Applied pure shear stress states

As we will be considering an array of variables including solute composition, stress orientation, and stress magnitude, we will simplify the analysis by focusing on a few shear stress orientations. We consider a LC configuration such as that shown in Fig. 2(a). In this configuration, three partial dislocations are present: the stair-rod partial dislocation (SRP) which lies on a (100) plane with a Burgers vector of  $\frac{a}{6}[011]$ , a Shockley partial dislocation (SP1) which lies on one of the {111} planes intersecting the (100) plane and is connected to SRP through a short intrinsic stacking fault, and another Shockley partial dislocation (SP2) which lies on the other {111} plane intersecting the (100) plane and is connected to SRP through a long intrinsic stacking fault. SP1 and SP2 have Burgers vectors of either  $\frac{a}{6}[211]$  or  $\frac{a}{6}[\bar{2}11]$ , depending on if the dislocation is to the left or right of SRP, respectively.

We consider a pure shear state, represented by the following stress tensor in the supercell basis (the  $x$  direction, which is represented by [011] in the crystal basis, is represented by [100] in the supercell basis):

$$\Sigma = \begin{bmatrix} -\sigma & 0 & 0 \\ 0 & \sigma & 0 \\ 0 & 0 & 0 \end{bmatrix}. \quad (5)$$

As the crystal is rotated counterclockwise (or, alternatively, the stress field is rotated clockwise) about the  $z$  axis by an angle  $\theta$ , the resulting stress field with respect to the crystal coordinates becomes

$$\Sigma' = Q\Sigma Q^T, \quad (6)$$

where  $Q$  is the rotation matrix:

$$Q = \begin{bmatrix} \cos\theta & \sin\theta & 0 \\ -\sin\theta & \cos\theta & 0 \\ 0 & 0 & 1 \end{bmatrix}. \quad (7)$$

The different partial dislocations will have a different Peach-Koehler (P-K) force as a function of  $\theta$ . The P-K force per unit length ( $\vec{F}^{PK}$ ) is defined as [29]

$$\vec{F}^{PK} = (\Sigma' \cdot \vec{b}) \times \vec{l}, \quad (8)$$

where  $\vec{b}$  is the Burgers vector and  $\vec{l}$  is the unit line direction of the dislocation. The normalized P-K forces (with  $\sigma$ ,  $|\vec{b}|$ , and  $|\vec{l}|$  set to one for each dislocation) are calculated and plotted in Fig. 2(b) for values of  $\theta$  between 0–90°, assuming SP1 to be to the left of SRP. In the supercell basis, the unit Burgers vectors for SRP, SP1, and SP2 are [100],  $Q^T(\theta = 54.74^\circ) \cdot [100]$ , and  $Q^T(\theta = -54.74^\circ) \cdot [100]$ , respectively, and the unit line direction is [001]. The value of  $\theta$  is taken as the angle between the Burgers vector of SRP with SP1 or SP2. Positive values for SP1 and SP2 represent motion toward SRP, while positive values for SRP represent motion to the right. The normalized P-K force on SRP is also equivalent to the normalized P-K force on the compact L dislocation (the absolute P-K force will be three times larger for the L dislocation than SRP as the magnitude of its Burgers vector is three times larger). The varying P-K forces will result in different responses of L and LC dislocations under applied stresses with different values of  $\theta$ . To simplify for further analysis, we consider five values of  $\theta$ : 0.5°, where SRP has a P-K force near zero and SP2 has a slightly higher P-K force than SP1, 9.74°, where SP2 has its maximum normalized P-K force, 35.26°, where SP1 has a P-K force of zero, 45°, where SRP has its maximum normalized P-K force, and 90°, where both SP1 and SP2 want to move away from SRP, which has a P-K force of zero. We will explore the effect of stresses given by Eq. (6) at these

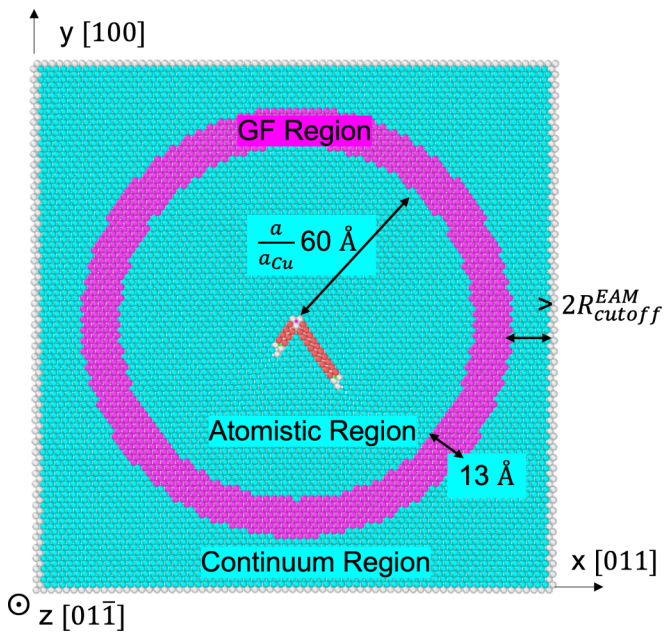


FIG. 3. The simulation cells used for relaxing L and LC dislocations are represented by this example for a fully relaxed LC dislocation in pure Cu in the same orientation as Fig. 2. The directions are given in the crystal basis. The region highlighted in magenta represents the GF region. Atoms colored in cyan, red, and grey represent FCC, HCP, and other environments according to the common neighbor analysis scheme [30] as implemented in OVITO [31].

orientations through the methodology presented in the next section.

### B. Computational details

We employ atomistic simulations using flexible boundary conditions, as described in Ref. [32], to model L and LC dislocations. The setup of the simulations is shown in Fig. 3. The supercell is partitioned into three regions: an inner atomistic region, an outer continuum region, and a buffer Green's function (GF) region. The atomistic region has a radius of 60 Å for pure Cu, and is scaled based on the lattice constant for other compositions. The GF region has a thickness of 13 Å, which is larger than twice the cutoff of the EAM potential ( $R_{\text{cutoff}}^{\text{EAM}}$ ), and the distance between the boundary of the GF region to the surface of the continuum region is larger than  $2R_{\text{cutoff}}^{\text{EAM}}$ . The thickness of the cell in the  $z$  direction (the dislocation line direction) is  $a/\sqrt{2}$ . Periodic boundary conditions are applied along the  $z$  direction, simulating an infinitely straight dislocation. All atoms are initially displaced according to the anisotropic linear elasticity theory solution for displacements around a L dislocation centered in the atomistic region using the BABEL package [33]. The atomistic region is then relaxed using the FIRE algorithm [34,35] as implemented in LAMMPS [36] with a force tolerance of  $10^{-7}$  eV/Å or until 100 000 minimization steps are reached (the maximum two-norm of the global force vector in the atomistic region from these cases is  $1.34 \times 10^{-5}$  eV/Å). Following this step, forces on atoms in the GF region are output for GF relaxation. With these forces, the positions of all atoms in the cell are updated through

the addition of displacements obtained from the following relation [32]:

$$u_i^m = \sum_n G_{ij}(\mathbf{r}^{mn}) f_j^n, \quad (9)$$

where  $f_j^n$  is the force in the  $j$  direction on atom  $n$  in the GF region,  $u_i^m$  is the resulting displacement in the  $i$  direction for atom  $m$ , and  $G_{ij}$  is the GF which maps  $f_j^n$  to a displacement as a function of  $\mathbf{r}^{mn}$ , the vector between the positions of atoms  $m$  and  $n$ . The relaxation process starting from the atomistic relaxation step is repeated until the magnitude of forces on each atom in the GF region are less than  $10^{-5}$  eV/Å or after 15 total iterations have been exceeded. The maximum force magnitude on an atom in the GF region in the latter case has a wide range of values and is discussed further in the Results section. Reaching the maximum number of iterations occurs due to dislocations approaching, or in some cases gliding into, the GF region, which is an inevitable consequence of using a finite sized supercell. Cases where this occurs will be discussed below in relation to trends at lower stresses and other compositions.

The use of this approach requires  $G_{ij}(\mathbf{r}^{mn})$  to be evaluated. As the setup of the simulation results in a two-dimensional problem, forces in the GF region are treated as line forces. For a sufficiently large  $|\mathbf{r}^{mn}|$ ,  $G_{ij}(\mathbf{r}^{mn})$  for a line force can be evaluated through the use of anisotropic linear elasticity theory [37]. However, as  $|\mathbf{r}^{mn}|$  tends to 0,  $G_{ij}(\mathbf{r}^{mn})$  must be evaluated using an interatomic potential. Therefore, we express  $G_{ij}(\mathbf{r}^{mn})$  as

$$G_{ij}(\mathbf{r}^{mn}) = \begin{cases} G_{ij}^{\text{el}}(\mathbf{r}^{mn}), & |\mathbf{r}^{mn}| \geq R_{\text{cutoff}}^{\text{GF}} \\ G_{ij}^{\text{lat}}(\mathbf{r}^{mn}), & |\mathbf{r}^{mn}| < R_{\text{cutoff}}^{\text{GF}} \end{cases} \quad (10)$$

where  $G_{ij}^{\text{el}}(\mathbf{r}^{mn})$  is the elastic GF,  $G_{ij}^{\text{lat}}(\mathbf{r}^{mn})$  is the lattice GF, and  $R_{\text{cutoff}}^{\text{GF}}$  is an imposed cutoff representing the minimum value of  $|\mathbf{r}^{mn}|$  before the elastic GF can be used. The elastic GF is calculated following Ref. [37], which only requires the anisotropic elastic constants (rotated to the desired orientation of the crystal) and the lattice constant as input. While there are various ways to calculate the lattice GF [38–40], we choose to follow a similar procedure as that found in Ref. [32] due to its simplicity. A perfect lattice in the same orientation as Fig. 3 is created with a length of approximately 40 Å in the  $x$  and  $y$  directions, and a thickness in the  $z$  direction of  $a/\sqrt{2}$ . A fixed line force of  $5 \times 10^{-6}$  eV/Å<sup>2</sup> in either the  $x$ ,  $y$ , or  $z$  direction is applied on the center atom. Resulting displacements on all other atoms are applied using the elastic GF. Maintaining a fixed force on the center atom, a region within a 20 Å radius of the center atom is relaxed using LAMMPS below a  $10^{-7}$  eV/Å force tolerance. Using the resulting displacements and the force on the center atom, the lattice GF as a function of  $\mathbf{r}^{mn}$  is tabulated using Eq. (9) with  $R_{\text{cutoff}}^{\text{GF}}$  set to  $5a/a_{\text{Cu}}$  Å, where  $a_{\text{Cu}}$  is the lattice constant for pure Cu. We chose this value as it is similar in magnitude to that used in previous work [32], although it should be mentioned that the error of the elastic GF compared to the lattice GF scales with  $(1/R_{\text{cutoff}}^{\text{GF}})^2$  [38]. In the dislocation geometry, we assume that the lattice GF can be approximated by that obtained from the perfect lattice, and use a lattice GF value corresponding to the best matching  $\mathbf{r}^{mn}$



vector between two atoms. We found that the predicted LC dislocation core structure for pure Cu using GFs obtained in this way agreed with the converged core structure obtained from a fixed boundary condition method with increasing system size (see Supplemental Material, Fig. S1 [41]).

To apply a desired stress state  $\Sigma'$ , displacement gradients are applied according to the following linear elasticity relation:

$$(u_{i,j} + u_{j,i})/2 = \epsilon_{ij} = S_{ijkl} \Sigma'_{kl}, \quad (11)$$

where  $u_{i,j}$  is a component of a displacement gradient tensor (where  $u_{i,j} = u_{j,i} = \epsilon_{ij}$  for pure shear, as all components of the infinitesimal rotation tensor are zero [42]),  $\epsilon_{ij}$  is a component of the strain tensor, and  $S_{ijkl}$  is a component of the compliance tensor, which is obtained from an inversion of the elastic constant tensor. Displacements ( $u_i^m$ ) corresponding to the displacement gradient ( $u_i^m = u_{i,j} r_j^m + C_i$ , where  $r_j^m$  is the reference position of atom  $m$  in the  $j$  direction and  $C_i$  is a constant set to keep the atoms within the simulation box) with  $\sigma$  equal to 100 MPa and a given value of  $\theta$  are added to the reference unstressed, relaxed configuration. The resulting structure is then relaxed through the approach described above, and if the GF region force criterion is met, displacements corresponding to the same displacement gradient are added by treating the new relaxed structure as the reference state. Assuming linear elasticity holds, the addition of these new displacements increases the applied value of  $\sigma$  by 100 MPa. This procedure is iterated until a given configuration reaches the maximum number of GF relaxation iterations. We assume that the GF does not change significantly under the applied stresses in this study. To avoid the possibility of atoms coming in and out of the region defined by  $R_{\text{cutoff}}^{\text{GF}}$ , we change the criteria for the application of the lattice GF in Eq. (10) to be

$$\frac{(r_x^{mn})^2}{[(1 + \epsilon_{11})R_{\text{cutoff}}^{\text{GF}}]^2} + \frac{(r_y^{mn})^2}{[(1 + \epsilon_{22})R_{\text{cutoff}}^{\text{GF}}]^2} < 1. \quad (12)$$

Instead of a circular cutoff as represented by Eq. (10), the above equation represents the resulting ellipse when the system is strained in the  $x$  and  $y$  directions ( $\epsilon_{11}$  and  $\epsilon_{22}$ , respectively).

We choose to investigate Cu-Ni solid solutions between 0–100 at.% Ni in increments of 10%. This system is chosen because it allows for the monotonic change of a low-stacking fault energy system (Cu) to a high-stacking fault energy system (Ni) with an increase in Ni. In an actual alloy, the GF will be a function of atom type, and any response to stress will become dependent on the dislocation length. Since the intent of the current study is to understand general trends, we circumvent these complications by making use of an average-atom representation of the Cu-Ni alloy through appropriate averaging of the EAM potential [28], as described in Ref. [27]. Using the average-atom description, we calculate lattice and elastic constants for each composition to carry out the above procedures for relaxation. We also calculate stable and unstable stacking fault energies to gain insight into the behavior of these dislocations. These, along with results of the dislocation relaxations, are reported in the next section.

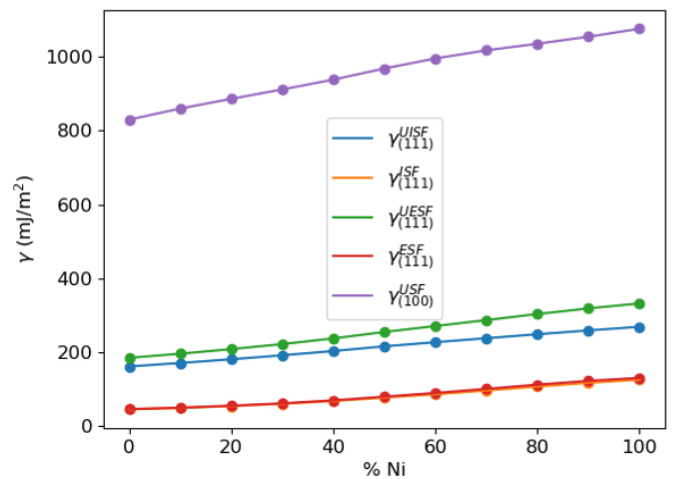


FIG. 4. Calculated stacking fault energies for the Cu-Ni average-atom alloy systems. The symbols in the legend are defined in Sec. III A.

### III. RESULTS

#### A. Material properties

Figure 4 displays the calculated stacking fault energies for the Cu-Ni average-atom alloys. The results show that the addition of Ni causes the stacking fault energies to increase. We have calculated five different stacking fault energies: the unstable and stable intrinsic stacking fault energies ( $\gamma_{(111)}^{\text{USF}}$  and  $\gamma_{(111)}^{\text{SF}}$ ) on the (111) plane, the unstable and stable extrinsic stacking fault energies ( $\gamma_{(111)}^{\text{ESF}}$  and  $\gamma_{(111)}^{\text{ESF}}$ ) on the (111) plane, and the unstable stacking fault energy ( $\gamma_{(100)}^{\text{USF}}$ ) on the (100) plane. Lower values of  $\gamma_{(111)}^{\text{SF}}$  are expected to favor the dissociated LC structure relative to the compact L structure. The lower the value of  $\gamma_{(111)}^{\text{ESF}}$ , the more we would expect an extrinsic fault (or nanotwin) to be able to nucleate from the dislocation under the appropriate applied stress. The lower the value of  $\gamma_{(100)}^{\text{USF}}$ , the easier it would be for a compact L dislocation to glide. Of course, the actual details of such scenarios depend on the core structure as shown in the following subsections.

The lattice and elastic constants of the average alloys are displayed in Fig. S2 in the Supplemental Material [41]. The results show that with the addition of Ni, the lattice constant decreases, while the elastic constants increase.

#### B. Equilibrium core structures

The equilibrium core structures at their unstressed state for all compositions relaxed to the force convergence criterion. Figure 5 shows the structure of the dislocation cores found in pure Cu, Cu-30% Ni, Cu-40% Ni, and pure Ni. As can be clearly seen, intrinsic stacking faults (colored in red in Fig. 5) are not present at compositions above 30% Ni. This suggests a transition between LC to L dislocations in a region between 30–40% Ni. Note that whether or not SP2 is to the right or left of the SRP for a LC dislocation depends on slight differences of where the center of the linear elasticity solution is placed with respect to the lattice. The LC dislocation being the stable configuration in pure Cu and the L dislocation being the stable

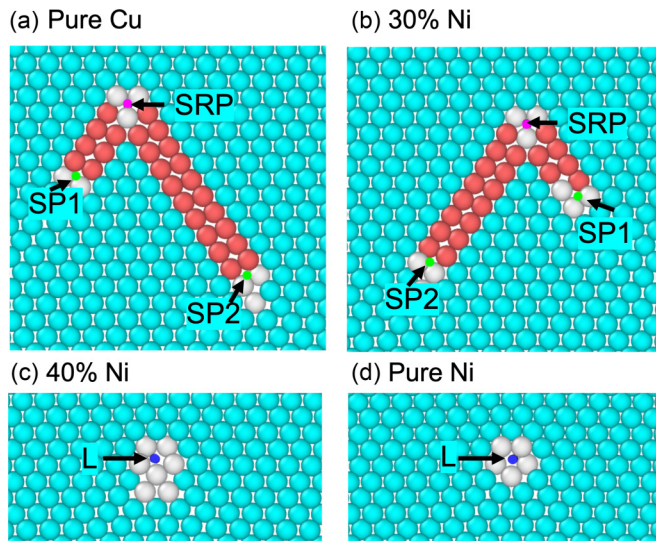


FIG. 5. Relaxed equilibrium core structures for (a) pure Cu, (b) Cu-30% Ni, (c) Cu-40% Ni, and (d) pure Ni. Atoms are colored similar to Fig. 3. Colored dots near grey atoms represent the end of dislocation lines found by the DXA algorithm [44] as implemented in OVITO [31]. The green, magenta, and blue dots represent SP1/SP2, SRP, and L dislocations, respectively.

configuration in pure Ni is in agreement with results from Ref. [43] using different potentials for the pure elements.

The LC configurations present in 0–30% Ni are all asymmetric, in agreement with elasticity predictions [20,21]. However, the ratio of the distance between SP2 and SRP ( $d_2$ ) to the distance between SP1 and SRP ( $d_1$ ) using elasticity theory is predicted to be 3.82, independent of the material system. Using the DXA algorithm [44], we find the  $d_2/d_1$  ratio to be 2.36, 2.34, 2.11, and 1.92 for the pure Cu, Cu-10% Ni, Cu-20% Ni, and Cu-30% Ni systems, respectively. This seems to be due to a decrease in  $d_2$  with increasing  $\gamma_{(111)}^{\text{ISF}}$  (45 to 60  $\text{mJ/m}^2$ ), as  $d_1$  maintains a value of approximately 9.8 Å across these systems. Ref. [19] found the  $d_2/d_1$  ratio to be 3.4 and 3.6 when modeling LC dislocations in pure Cu and Ag, respectively. The value of  $\gamma_{(111)}^{\text{ISF}}$  from the interatomic potentials used in Ref. [19] was calculated to be 36  $\text{mJ/m}^2$  for Cu and 23  $\text{mJ/m}^2$  for Ag. The potential used in the present paper results in a  $\gamma_{(111)}^{\text{ISF}}$  value of 45  $\text{mJ/m}^2$  for Cu. Thus it is expected that the linear elasticity description for the LC structure is only applicable in the limit of low values of  $\gamma_{(111)}^{\text{ISF}}$ . Otherwise, the calculation of an accurate dislocation core structure requires atomistic modeling to capture near-core effects.

We further analyze the core structures by looking at differential displacement (DD) maps [45] for pure Cu and pure Ni as shown in Fig. S3 in the Supplemental Material [41]. For Cu, three different projections are shown corresponding to the Burgers vectors of the different partial dislocations in the LC configuration. For Ni, the three different projections include the two Shockley partial dislocation Burgers vectors of the LC configuration, and the Burgers vector of the L dislocation. While the L configuration in pure Ni does not show any intrinsic stacking faults in Fig. 5(d) [the value of  $\gamma_{(111)}^{\text{ISF}}$  for pure Ni is 125  $\text{mJ/m}^2$ ], the DD maps show the

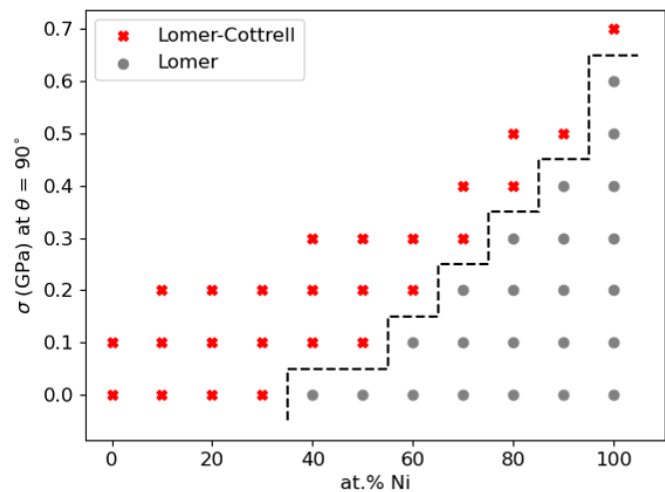


FIG. 6. Dislocation states at a given value of  $\sigma$  and Ni content for a pure shear stress state with  $\theta$  equal to  $90^\circ$ . The top data point at each composition reached the maximum number of GF iterations. The black dashed line represents a boundary between different dislocation states.

presence of displacements associated with the projection of Shockley partial dislocation Burgers vectors in a  $(\bar{1}11)$  or  $(111)$  plane just under the L dislocation. The small amount of core spreading in these planes appears to impact the response of the core under certain stress states, as will be discussed further below.

### C. Effect of an applied shear stress

Here we present the results of applying different stresses on L/LC dislocations in the order of orientations that show the simplest responses. Simulations are terminated when the GF iterations exceeds 15 total iterations. As discussed above, we find that this occurs when a partial or full dislocation moves close to the GF region, as shown in Fig. S4 [41], which can occur both at relatively low or high stresses depending on the available core states. The range of the maximum magnitude of the force in the GF region is given for each value of  $\theta$  below. The resulting core structures are classified using the DXA algorithm [44]. Note that before applying any stress, SP2 is to the right of SRP for 0–20% Ni, while for 30% Ni SP2 is to the left of SRP. Accounting for this, a value of  $-\theta$  was used for 30% Ni for the cases where  $\theta$  equals  $9.74^\circ$ ,  $45^\circ$ , and  $35.26^\circ$  to be consistent with the P-K force values in Fig. 2(b). However, we tested  $+/-$  values of  $\theta$  for the mentioned angles for 0–30% Ni and did not find significant differences in the results.

#### 1. Pure shear with $\theta = 90^\circ$

The results for a pure shear stress state with  $\theta$  equal to  $90^\circ$  are shown in Fig. 6. Each column in the plot represents a composition, and each row represents a value of  $\sigma$ . The different symbols represent different states of the dislocation as described in the legend. In this scenario, dislocations that start as LC configurations at zero stress remain in the LC configuration, while dislocations that start as L configurations transition to the LC configuration at a high enough stress.

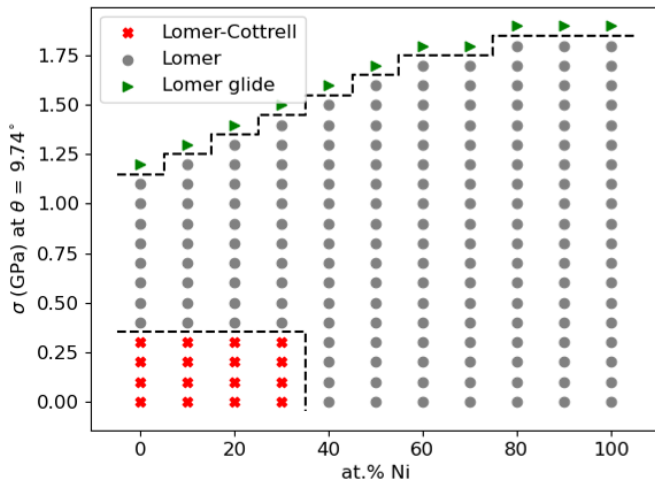


FIG. 7. Dislocation states at a given value of  $\sigma$  and Ni content for a pure shear stress state with  $\theta$  equal to  $9.74^\circ$ . The top data point at each composition reached the maximum number of GF iterations. The black dashed lines represent boundaries between different dislocation states.

This occurs because the P-K force on SP1 and SP2 favors motion away from SRP, which has a P-K force of zero at this value of  $\theta$ . The stress at which this transition occurs increases with increasing Ni content, which makes intuitive sense as the values of  $\gamma_{(111)}^{\text{ISF}}$  and  $\gamma_{(111)}^{\text{USF}}$  increase with Ni content.

The maximum magnitude of a force vector on an atom in the GF region at the terminated state ranged from  $1.1 \times 10^{-5}$  eV/Å to  $3.3 \times 10^{-3}$  eV/Å. These forces are relatively small and are not expected to have a significant effect on the final core structure. Additionally, the final core structure of the terminated states being LC dislocations is consistent with the trend of the converged calculations in Fig. 6.

### 2. Pure shear with $\theta = 9.74^\circ$

The results for a pure shear stress state with  $\theta$  equal to  $9.74^\circ$  are shown in Fig. 7. In this scenario, dislocations that start as L configurations at zero stress remain in the L configuration until a high enough stress is reached where the dislocation begins to glide away from its initial position on the (100) plane. Dislocations that start as LC configurations at zero stress eventually transition into a L configuration with increasing stress, and eventually glide on the (100) plane. This occurs because the P-K force on both SP1 and SP2 drives them to combine with SRP to form a L configuration, which has a nonzero P-K force for glide. The stress at which glide on the (100) plane occurs increases with increasing Ni content, which makes intuitive sense as the value of  $\gamma_{(100)}^{\text{USF}}$  increases with Ni content.

The maximum magnitude of a force vector on an atom in the GF region at the terminated state ranged from  $2.8 \times 10^{-3}$  eV/Å to  $5.2 \times 10^{-2}$  eV/Å. As all of the terminated states at this value of  $\theta$  result in a L dislocation gliding toward the GF region (which begins early on in the GF relaxation cycle), the forces at the GF region do not change the conclusion that the dislocation is expected to glide in an infinite medium.

### 3. Pure shear with $\theta = 45^\circ$

The results for a pure shear stress state with  $\theta$  equal to  $45^\circ$  are shown in Fig. 8(a). In this scenario, dislocations that start as LC configurations at zero stress remain in the LC configuration. For Ni concentrations in the range of 40 – 80%, there is a transformation from an initial L configuration to a LC configuration, and the stress at which this transition occurs increases with increasing Ni content. The resulting LC configurations are strongly asymmetrical, as there are opposite driving forces at  $\theta = 45^\circ$  for SP1 and SP2 as shown in Fig. 2(b). However, above 80% Ni, the L dislocations glide on the (100) plane instead of transforming into a LC configuration. Surprisingly, the stress at which this occurs for 100% Ni is lower than that for 90% Ni, which is also lower than the stress for the L to LC transition at 80% Ni.

To investigate the reason for this, we analyze the L core structure in more detail. Specifically, we consider three atoms [colored in black in the inset of Fig. 8(b)]. The first atom (A), is the atom near the bottom of the core. The other two atoms (B and C) are to the left and right of A, respectively. These atoms are chosen because they are close to the core and because the A-B atom pair and A-C atom pair each bound one of the two {111} planes that the dislocation can spread in. We define a core asymmetry parameter as a function of stress ( $\lambda(\sigma)$ ) as

$$\lambda(\sigma) = \frac{|d_{AB}(\sigma)| - |d_{AC}(\sigma)|}{a} \quad (13)$$

where  $d_{AB}(\sigma)$  and  $d_{AC}(\sigma)$  represent the distance of atoms B and C, respectively, to atom A at a given value of  $\sigma$ . This parameter describes how much the dislocation core is spread in the plane between atoms A and B compared to the plane between atoms A and C. We track this parameter while the dislocation core remains in the static L configuration at compositions of 80%, 90%, and 100% Ni [shown in Fig. 8(b)]. For 80% Ni, we find that  $\lambda(\sigma)$  monotonically increases with  $\sigma$ . This is consistent with the fact that this structure will eventually transform into a strongly asymmetric LC structure with the largest stacking fault present in the plane between atoms A and B. For 90% and 100% Ni,  $\lambda(\sigma)$  initially increases with  $\sigma$  until a maximum is reached, after which the value begins to decrease. The maximum for 100% Ni is smaller than that for 90% Ni and seems to appear at a lower value of  $\sigma$  than the maximum for 90% Ni. This can be rationalized through the fact that a higher amount of Ni content results in higher values of  $\gamma_{(111)}^{\text{UISF}}$  and  $\gamma_{(111)}^{\text{ISF}}$ , so it is increasingly difficult to have core spreading in the {111} planes, which is why a LC configuration is not observed at the 90% and 100% Ni compositions. When there is more core spreading in {111} planes, it becomes difficult for the dislocation to glide on the (100) plane, even though this orientation represents the maximum normalized P-K force for glide on the (100) plane. This is why the L dislocation at 100% Ni glides at a lower stress than at 90% Ni. This situation represents a competition in normalized P-K forces and fault energies for different planes.

The maximum magnitude of a force vector on an atom in the GF region at the terminated state below 80% Ni ranged from  $1.0 \times 10^{-5}$  eV/Å to  $1.7 \times 10^{-3}$  eV/Å. These relatively low values, as well as the trend in Fig. 8(a), suggest that the LC core structure should still be the expected configuration



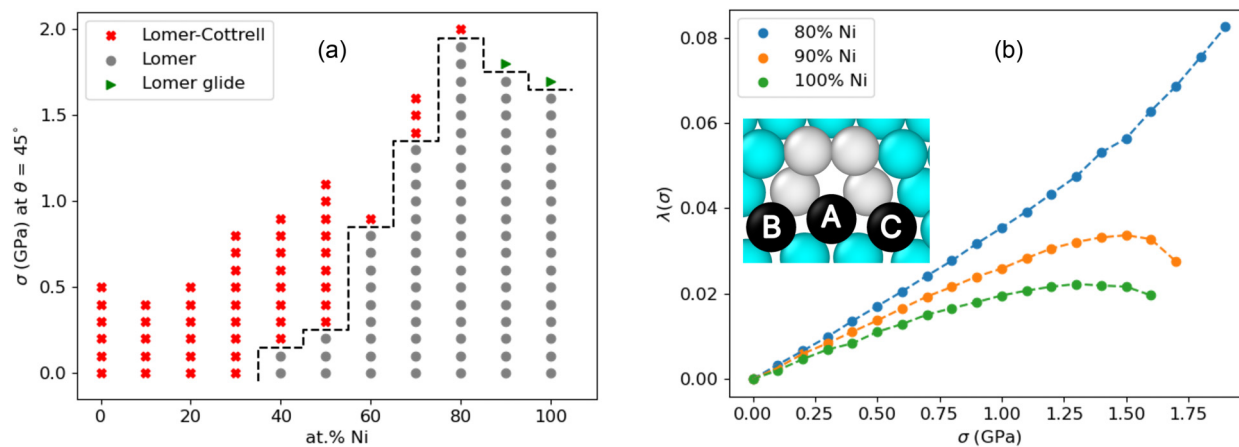


FIG. 8. (a) Dislocation states at a given value of  $\sigma$  and Ni content for a pure shear stress state with  $\theta$  equal to  $45^\circ$ . The top data point at each composition reached the maximum number of GF iterations. The black dashed line represents a boundary between dislocation states. (b) Values of the core asymmetry parameter defined in Eq. (13) as a function of stress for 80%, 90%, and 100% Ni. Inset: View of a L dislocation core where the black atoms are the atoms considered for the core asymmetry parameter.

at the given values of  $\sigma$  of the terminated states. At 80% Ni and above, these values ranged from  $1.8 \times 10^{-2}$  eV/Å to  $5.2 \times 10^{-2}$  eV/Å. For 80% Ni, this is due to one of the partial dislocations belonging to the LC core approaching very close to the GF region. A LC core structure at this composition is still expected as it is consistent with the trend in  $\lambda(\sigma)$  with increasing  $\sigma$ . Glide above 80% Ni is also expected based on the trend in  $\lambda(\sigma)$ .

4. Pure shear with  $\theta = 35.26^\circ$

The results for a pure shear stress state with  $\theta$  equal to  $35.26^\circ$  are shown in Fig. 9(a). All cores that initially start in the L configuration at zero stress (as well as the 30% Ni configuration) glide on the (100) plane when  $\sigma$  equals 1.5 GPa. We expect that the reason for this lack of dependence on Ni content is due to a similar effect as in the previous case, which is that for lower Ni content, there is more core spreading in {111} planes, making it difficult for the core to stay compact enough to glide on the (100) plane except at higher stresses. For higher Ni content, there is less core spreading, but the

barrier to glide on the (100) plane is higher. These effects cancel out at this value of  $\theta$  leading to a constant glide stress in the range of 30–100% Ni.

All cores that start in a LC configuration transition into a configuration similar to that shown in Fig. 9(b), where the partial dislocation colored in light blue represents a Frank partial dislocation (with a Burgers vector of  $\frac{a}{3}\langle 111 \rangle$ ) as identified by the DXA algorithm [44]. With further applied stress, cores at 0% and 10% Ni transform into an obtuse configuration, similar to the configuration shown in Fig. 9(c), where the yellow partial represents a Hirth partial dislocation (with a Burgers vector of  $\frac{a}{3}\langle 100 \rangle$ ) as identified by the DXA algorithm. The upper fault in Fig. 9(c) contains an extrinsic stacking fault, or a nanotwin. The transition from an acute lock to an obtuse lock with an extrinsic stacking fault shares similarities with the findings in a study by Baskes *et al.* [46], where the authors strain an initially obtuse lock and find an intermediate state of an acute lock with an extrinsic stacking fault. The Burgers vector of the partial dislocation at the apex of their acute lock is  $\frac{a}{6}[011]$  (a stair-rod partial dislocation), and that

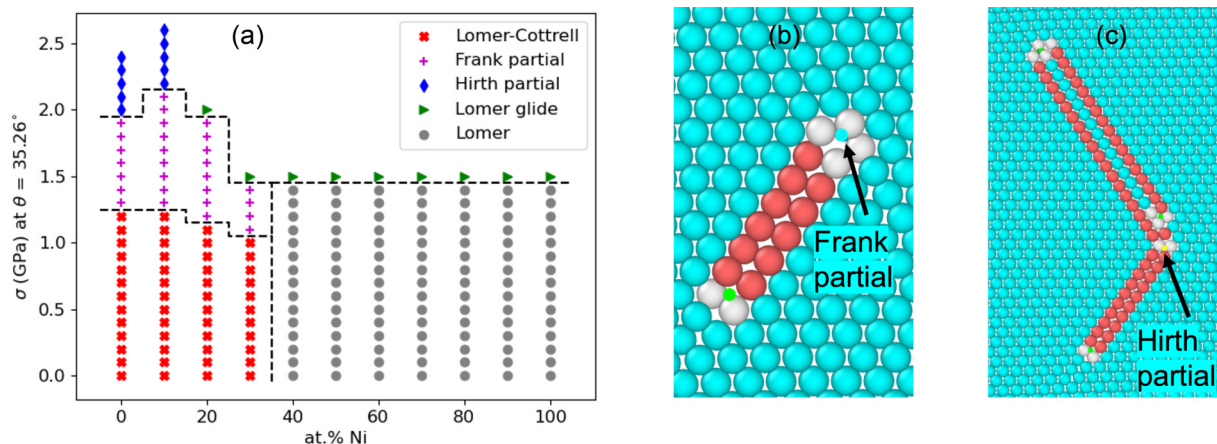


FIG. 9. (a) Dislocation states at a given value of  $\sigma$  and Ni content for a pure shear stress state with  $\theta$  equal to  $35.26^\circ$ . The top data point at each composition reached the maximum number of GF iterations. The black dashed lines represent boundaries between dislocation states. (b) Core structure at 0% Ni and  $\sigma$  equal to 1.9 GPa, and (c) 2.0 GPa.



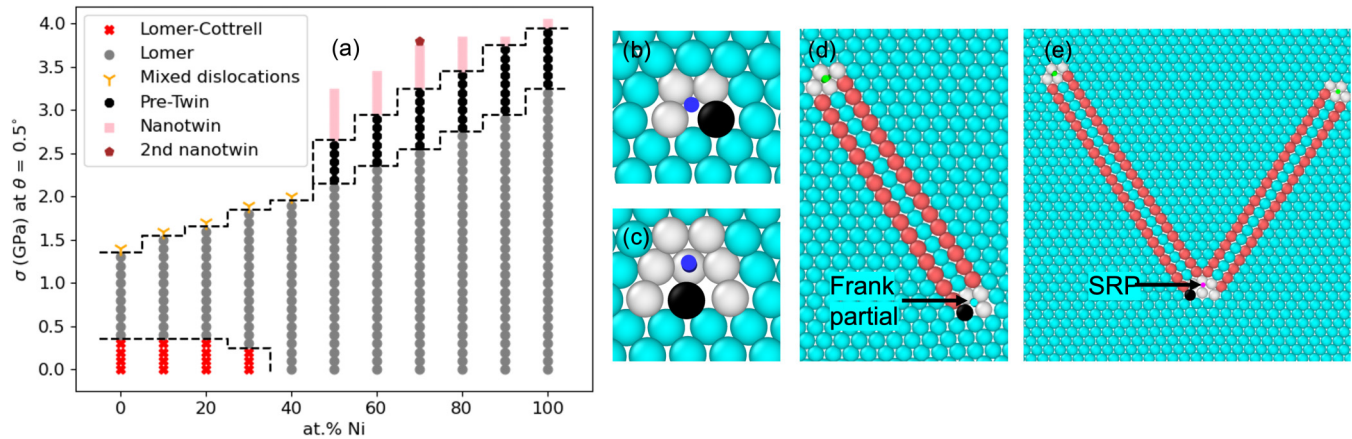


FIG. 10. (a) Dislocation states at a given value of  $\sigma$  and Ni content for a pure shear stress state with  $\theta$  equal to  $0.5^\circ$ . The top data point at each composition reached the maximum number of GF iterations. The black dashed lines represent boundaries between dislocation states. (b) Core structure at 70% Ni and  $\sigma$  equal to 2.5 GPa, (c) 2.6 GPa, (d) 3.3 GPa, and (e) 3.8 GPa. The black atom is highlighted to show the transition of the L core in (b) to the intermediate state in (c).

of the partial dislocation at the apex of their obtuse lock is  $\frac{a}{3}[100]$  (a Hirth partial dislocation). This suggests that these locks are related to each other by the removal or addition of an extrinsic stacking fault. For 20% and 30% Ni, the state with a Frank partial dislocation does not transition into an obtuse lock with further applied stress, but instead eventually glides on the (100) plane. We expect that this is due to a competition between  $\gamma_{(111)}^{\text{ESF}}$  to form the obtuse configuration and  $\gamma_{(100)}^{\text{USF}}$  for glide on the (100) plane.

The maximum magnitude of a force vector on an atom in the GF region at the terminated state for 0% and 10% Ni was  $2.8 \times 10^{-2}$  eV/Å and  $5.4 \times 10^{-3}$  eV/Å, respectively. The obtuse configuration of these terminated states are just extended structures of the similar states found at smaller values of  $\sigma$ , so the obtuse configuration is still expected at the terminated state. Above 10% Ni, the maximum magnitude of the force vectors range from  $1.8 \times 10^{-3}$  eV/Å to  $1.3 \times 10^{-1}$  eV/Å. As these states represent the glide of a L dislocation, the expected state would still be a continuous glide.

### 5. Pure shear with $\theta = 0.5^\circ$

The results for a pure shear stress state with  $\theta$  equal to  $0.5^\circ$  are shown in Fig. 10(a). All cores that initially start in the LC configuration at zero stress transition into the L configuration, and eventually emit two dissociated mixed dislocations. At 40% Ni, the final state is an emission of two mixed dislocations as well. For dislocations that start in the L configuration at 50% Ni or more, a transformation occurs that results in an extrinsic stacking fault/nanotwin with a Frank partial dislocation as shown in Fig. 10(d). This is confirmation of the proposed twin nucleation mechanism from a L dislocation as mentioned in Refs. [12,13]. There is a large jump in stress required for the emission of mixed dislocations at 40% Ni and the creation of a nanotwin at 50% Ni. This is because before creating a nanotwin, the L core at 50% Ni and above begins to glide on the (100) plane but becomes stuck in an intermediate state [Fig. 10(c)]. This intermediate state [labeled as pretwin in Fig. 10(a)] prevents the emission of mixed dislocations, and eventually a nanotwin is nucleated. The small nonzero value

of  $\theta$  gives a small driving force for glide in the (100) plane to access the intermediate state, as well as a stronger driving force for nanotwin nucleation to the left of the core than to the right.

For 70% Ni, there is a further transformation observed where a second nanotwin is nucleated to the right of the core as shown in Fig. 10(e), with the Frank partial dislocation transitioning into a stair-rod partial. Presumably, if the cell sizes were larger, this second nanotwin would nucleate for other compositions in the range of 50%–100% Ni, as there is a driving force to do so. The reason this does not occur for these compositions is due to the partial dislocation associated with the first nanotwin approaching the GF region, which results in the simulation terminating after a maximum number of iterations.

The maximum magnitude of a force vector on an atom in the GF region at the terminated state below 50% Ni ranged from 0.30 eV/Å to 1.7 eV/Å. This is due to the mixed dislocations in these states entering the GF region. In an infinite environment, it is expected that the mixed dislocations will continue to glide, especially since this starts early on in the GF relaxation cycle. For 50% Ni, the maximum force magnitude is 0.18 eV/Å. While this is high, the state remains a nanotwin similar to the states found at lower values of  $\sigma$ . For compositions above 50%, the maximum force magnitude ranged from  $1.3 \times 10^{-5}$  eV/Å to  $1.2 \times 10^{-3}$  eV/Å, which are relatively low values. Additionally, the terminated states represent the formation of a nanotwin, which is consistent with the trend of the converged calculations in Fig. 10(a).

## IV. DISCUSSION

From the presented simulation results, it is clear that L and LC dislocations can attain a number of different configurations depending on the composition and applied shear stress state. We find that L dislocations can readily transform into LC configurations and vice versa. The ability for a LC dislocation to transform to a L configuration is in agreement with the analysis by Stroh [22] as well as TEM observations of glide on the (100) plane in a Cu-Al alloy, which has lower

fault energies than pure Cu [26]. Additionally, the stresses at which glide on the (100) plane can occur at  $\theta$  equal to  $9.74^\circ$  is lower for compositions that start with a LC configuration than for compositions that start with a L configuration. This suggests that the presence of a sessile SRP does not guarantee a stronger barrier against glide compared to the glissile L dislocation and that the role of fault energies are important. However, this depends on the value of  $\theta$ , as for the cases where  $\theta$  equals  $45^\circ$  or  $35.26^\circ$ , dislocations in environments with a higher Ni content began to glide while dislocations with lower Ni concentrations did not. The orientation dependence of the glide of these dislocations may play a role in the orientation dependence of work hardening in single-crystal FCC alloys [4,5].

The orientation dependence of work hardening in FCC alloys may also be influenced by the orientation dependence of twin formation. We find the L and LC dislocations can nucleate an extrinsic stacking fault, or a nanotwin, when  $\theta$  is equal to  $0.5^\circ$  or  $35.26^\circ$ . The values of  $\sigma$  to form a nanotwin at these orientations are quite high, beyond the values likely to be measured in tensile stress-strain curves of FCC alloys (an exception to this is the 1.9 GPa tensile strength observed in a compositionally complex steel which exhibited twinning in the FCC matrix [47]). However, high internal stresses can be achieved through mechanisms such as planar slip of dislocations, which is also orientation dependent [5]. Short-range ordering or clustering of solutes can also promote planar slip through slip-plane softening [48] and through the suppression of cross-slip [49]. While it is plausible that a local stress concentration can provide a source for twin nucleation from L and LC dislocations, there are a variety of possible twinning mechanisms in FCC metals and alloys that could be activated [13].

A number of assumptions were required to carry out the present paper. We assumed that the stress state of the system could be described by linear elasticity, while in reality we are controlling the strain state. In pure Cu and Ni, we find that for high values of compressive and tensile strain in the  $x$  direction, the bulk system (without a dislocation) starts to deviate from linear elasticity (Fig. S5 in the Supplemental Material [41]). Accounting for this would require calculations of higher-order elastic constants. However, after measuring the stress state from the GF region of converged dislocation structures in LAMMPS, we found that other stress components did not have as strong of a deviation from the linear elasticity prediction (Fig. S6 in the Supplemental Material [41]).

We have also assumed that the behavior of the dislocations under stress can be captured using a two-dimensional simulation. Thus, any change in core structure occurs homogeneously along the dislocation line. Studying the same dislocation behavior in a three-dimensional system may al-

low for changes to occur through the formation of a critical nucleus of a bow-out configuration of a fault [22] or of a kink-pair facilitating L dislocation glide [14]. Additionally, since the difference in energy between a L and LC dislocation is expected to be small [19], at temperature the cores may exhibit a polymorphic structure along the dislocation line, analogous to that recently observed in simulations of  $\langle a \rangle$ -type screw dislocations in hexagonal Ti [50]. A local variation of composition may also lead to a polymorphic structure. Exploring the formation of a critical nucleus requires knowledge of the initial and final states, a polymorphic structure at temperature is more likely to be found in regions of stress-composition space near core transitions, and the effect of local composition variation could be linked to different core structures available at different compositions. All of these considerations will be greatly facilitated by and motivated by the different core structures mapped out as a function of applied stress and composition in the current paper.

## V. CONCLUSIONS

We have presented results of atomistic simulations of L and LC dislocations in model FCC Cu-Ni alloys modeled with an average-atom potential, under various compositional and stress environments using a flexible boundary condition approach. We observe a variety of transformations, including L to LC, L to (100) glide, LC to L to (100) glide, L to nanotwin (and double nanotwin) nucleation, and LC to an obtuse configuration with a nanotwin. The variety of transformations under different values and orientations of pure shear stress are expected to play a role in the orientation dependence of work hardening in FCC alloys.

## ACKNOWLEDGMENTS

The authors thank Robert Ritchie and Andrew Minor for useful discussions. This work was supported by the U.S. Department of Energy, Office of Science, Office of Basic Energy Sciences, Materials Science and Engineering Division, under Contract No. DE-AC02-05-CH11231, within the Damage Tolerance in Structural Materials. This work made use of computational resources provided by the Extreme Science and Engineering Discovery Environment (XSEDE), which is supported by National Science Foundation under Grant No. ACI-1548562, as well as use of the Savio computational cluster resource provided by the Berkeley Research Computing program at the University of California, Berkeley (supported by the UC Berkeley Chancellor, Vice Chancellor for Research, and Chief Information Officer). A.A. acknowledges a fellowship through the National Science Foundation Graduate Research Fellowship Program (Grant No. DGE 1752814).

- [1] W. M. Lomer, A dislocation reaction in the face-centred cubic lattice, *London, Edinburgh, Dublin Philos. Mag. J. Sci.* **42**, 1327 (1951).  
 [2] A. H. Cottrell, LX. The formation of immobile dislocations during slip, *London, Edinburgh, Dublin Philos. Mag. J. Sci.* **43**, 645 (1952).

- [3] J. Friedel, CXXX. On the linear work hardening rate of face-centred cubic single crystals, *London, Edinburgh, Dublin Philos. Mag. J. Sci.* **46**, 1169 (1955).  
 [4] B. Uzer, S. Picak, J. Liu, T. Jozaghi, D. Canadinc, I. Karaman, Y. Chumlyakov, and I. Kireeva, On the mechanical response and microstructure evolution of NiCoCr single

- crystalline medium entropy alloys, *Mater. Res. Lett.* **6**, 442 (2018).
- [5] S. Picak, J. Liu, C. Hayrettin, W. Nasim, D. Canadinc, K. Xie, Y. Chumlyakov, I. Kireeva, and I. Karaman, Anomalous work hardening behavior of  $\text{Fe}_{40}\text{Mn}_{40}\text{Cr}_{10}\text{Co}_{10}$  high entropy alloy single crystals deformed by twinning and slip, *Acta Mater.* **181**, 555 (2019).
- [6] X. D. Xu, P. Liu, Z. Tang, A. Hirata, S. X. Song, T. G. Nieh, P. K. Liaw, C. T. Liu, and M. W. Chen, Transmission electron microscopy characterization of dislocation structure in a face-centered cubic high-entropy alloy  $\text{Al}_{0.1}\text{CoCrFeNi}$ , *Acta Mater.* **144**, 107 (2018).
- [7] Y. Ma, F. Yuan, M. Yang, P. Jiang, E. Ma, and X. Wu, Dynamic shear deformation of a CrCoNi medium-entropy alloy with heterogeneous grain structures, *Acta Mater.* **148**, 407 (2018).
- [8] X. Gao, Y. Lu, J. Liu, J. Wang, T. Wang, and Y. Zhao, Extraordinary ductility and strain hardening of  $\text{Cr}_{26}\text{Mn}_{20}\text{Fe}_{20}\text{Co}_{20}\text{Ni}_{14}$  TWIP high-entropy alloy by cooperative planar slipping and twinning, *Materialia* **8**, 100485 (2019).
- [9] L. Qi, C. Q. Liu, H. W. Chen, and J. F. Nie, Atomic scale characterization of complex stacking faults and their configurations in cold deformed  $\text{Fe}_{42}\text{Mn}_{38}\text{Co}_{10}\text{Cr}_{10}$  high-entropy alloy, *Acta Mater.* **199**, 649 (2020).
- [10] J. Wang, H. Yang, H. Huang, J. Zou, S. Ji, and Z. Liu, High strength-ductility  $\text{Co}_{23}\text{Cr}_{23}\text{Ni}_{23}\text{Mn}_{31}$  medium-entropy alloy achieved via defect engineering, *Mater. Sci. Eng., A* **796**, 139974 (2020).
- [11] J. Cohen and J. Weertman, A dislocation model for twinning in f.c.c. metals, *Acta Metall.* **11**, 996 (1963).
- [12] I. Karaman, H. Sehitoglu, K. Gall, Y. I. Chumlyakov, and H. J. Maier, Deformation of single crystal Hadfield steel by twinning and slip, *Acta Mater.* **48**, 1345 (2000).
- [13] B. C. De Cooman, Y. Estrin, and S. K. Kim, Twinning-induced plasticity (TWIP) steels, *Acta Mater.* **142**, 283 (2018).
- [14] D. Rodney, Activation enthalpy for kink-pair nucleation on dislocations: Comparison between static and dynamic atomic-scale simulations, *Phys. Rev. B* **76**, 144108 (2007).
- [15] M. Carrard and J. L. Martin, A study of (001) glide in [112] aluminium single crystals II. Microscopic mechanism, *Philos. Mag. A* **58**, 491 (1988).
- [16] M. J. Mills and P. Stadelmann, A study of the structure of Lomer and  $60^\circ$  dislocations in aluminium using high-resolution transmission electron microscopy, *Philos. Mag. A* **60**, 355 (1989).
- [17] D. Hull and D. J. Bacon, *Introduction to Dislocations* (Elsevier, Kidlington, Oxford, OX5 1GB, 2011).
- [18] G. Saada and J. Douin, On the stability of dissociated dislocations, *Philos. Mag. Lett.* **64**, 67 (1991).
- [19] F. Gao and D. J. Bacon, On the structure and energy of dissociated dislocations in F.C.C. metals, *Philos. Mag. A* **66**, 839 (1992).
- [20] A. Korner, H. Schmid, and F. Prinz, Asymmetrical equilibrium positions and line tensions of composite dislocations, *Phys. Status Solidi A* **51**, 613 (1979).
- [21] J. Bonneville and J. Douin, On the asymmetrical dissociation of Lomer dislocations, *Philos. Mag. Lett.* **62**, 247 (1990).
- [22] A. N. Stroh, LI. The strength of Lomer-Cottrell sessile dislocations, *Philos. Mag.* **1**, 489 (1956).
- [23] V. B. Shenoy, R. V. Kukta, and R. Phillips, Mesoscopic Analysis of Structure and Strength of Dislocation Junctions in FCC Metals, *Phys. Rev. Lett.* **84**, 1491 (2000).
- [24] D. Rodney and R. Phillips, Structure and Strength of Dislocation Junctions: An Atomic Level Analysis, *Phys. Rev. Lett.* **82**, 1704 (1999).
- [25] A. Korner and H. P. Karnthaler, The study of glide dislocation loops on {001} planes in a f.c.c. alloy, *Philos. Mag. A* **42**, 753 (1980).
- [26] A. Korner and H. P. Karnthaler, Glide dislocations on cube planes in a low stacking-fault energy alloy, *Phys. Status Solidi A* **75**, 525 (1983).
- [27] C. Varvenne, A. Luque, W. G. Nöhring, and W. A. Curtin, Average-atom interatomic potential for random alloys, *Phys. Rev. B* **93**, 104201 (2016).
- [28] B. Onat and S. Durukanoğlu, An optimized interatomic potential for Cu-Ni alloys with the embedded-atom method, *J. Phys.: Condens. Matter* **26**, 035404 (2014).
- [29] P. M. Anderson, J. P. Hirth, and J. Lothe, *Theory of Dislocations* (Cambridge University Press, New York NY, USA, 2017).
- [30] A. Stukowski, Structure identification methods for atomistic simulations of crystalline materials, *Modell. Simul. Mater. Sci. Eng.* **20**, 045021 (2012).
- [31] A. Stukowski, Visualization and analysis of atomistic simulation data with OVITO—the Open Visualization Tool, *Modell. Simul. Mater. Sci. Eng.* **18**, 015012 (2010).
- [32] S. Rao, C. Hernandez, J. P. Simmons, T. A. Parthasarathy, and C. Woodward, Green's function boundary conditions in two-dimensional and three-dimensional atomistic simulations of dislocations, *Philos. Mag. A* **77**, 231 (1998).
- [33] E. Clouet, BABEL package, <http://emmanuel.clouet.free.fr/Programs/Babel/index.html>.
- [34] E. Bitzek, P. Koskinen, F. Gähler, M. Moseler, and P. Gumbsch, Structural Relaxation Made Simple, *Phys. Rev. Lett.* **97**, 170201 (2006).
- [35] J. Guérolé, W. G. Nöhring, A. Vaid, F. Houllé, Z. Xie, A. Prakash, and E. Bitzek, Assessment and optimization of the fast inertial relaxation engine (FIRE) for energy minimization in atomistic simulations and its implementation in LAMMPS, *Comput. Mater. Sci.* **175**, 109584 (2020).
- [36] S. Plimpton, Fast parallel algorithms for short-range molecular dynamics, *J. Comput. Phys.* **117**, 1 (1995).
- [37] A. N. Stroh, Steady state problems in anisotropic elasticity, *J. Math. Phys.* **41**, 77 (1962).
- [38] D. R. Trinkle, Lattice Green function for extended defect calculations: Computation and error estimation with long-range forces, *Phys. Rev. B* **78**, 014110 (2008).
- [39] M. Ghazisaeidi and D. R. Trinkle, Convergence rate for numerical computation of the lattice Green's function, *Phys. Rev. E* **79**, 037701 (2009).
- [40] Anne Marie Z. Tan and D. R. Trinkle, Computation of the lattice Green function for a dislocation, *Phys. Rev. E* **94**, 023308 (2016).
- [41] See Supplemental Material at <http://link.aps.org/supplemental/10.1103/PhysRevMaterials.6.103603> for further discussion and details associated with methodology and dislocation core structure.
- [42] L. Anand and S. Govindjee, *Continuum Mechanics of Solids* (Oxford University Press, Oxford, United Kingdom, 2020).



- [43] C. R. Weinberger and W. Cai, The stability of Lomer-Cottrell jogs in nanopillars, *Scr. Mater.* **64**, 529 (2011).
- [44] A. Stukowski and K. Albe, Extracting dislocations and non-dislocation crystal defects from atomistic simulation data, *Modell. Simul. Mater. Sci. Eng.* **18**, 085001 (2010).
- [45] V. Vitek, R. C. Perrin, and D. K. Bowen, The core structure of  $\frac{1}{2}(111)$  screw dislocations in b.c.c. crystals, *Philos. Mag.* **21**, 1049 (1970).
- [46] M. I. Baskes, R. G. Hoagland, and T. Tsuji, An atomistic study of the strength of an extended-dislocation barrier, *Modell. Simul. Mater. Sci. Eng.* **6**, 9 (1998).
- [47] Z. Wang, W. Lu, F. An, M. Song, D. Ponge, D. Raabe, and Z. Li, High stress twinning in a compositionally complex steel of very high stacking fault energy, *Nat. Commun.* **13**, 3598 (2022).
- [48] V. Gerold and H. P. Karnthaler, On the origin of planar slip in f.c.c. alloys, *Acta Metall.* **37**, 2177 (1989).
- [49] A. Abu-Odeh and M. Asta, Modeling the effect of short-range order on cross-slip in an FCC solid solution, *Acta Mater.* **226**, 117615 (2022).
- [50] M. Poschmann, I. S. Winter, M. Asta, and D. C. Chrzan, Molecular dynamics studies of a-type screw dislocation core structure polymorphism in titanium, *Phys. Rev. Mater.* **6**, 013603 (2022).